Applied Materials Today 27 (2022) 101457

Contents lists available at ScienceDirect

Applied Materials Today

journal homepage: www.elsevier.com/locate/apmt

Anisotropic magnetized tubular microrobots for bioinspired adaptive locomotion

Guanghui Yan[a,1], Borui Xu[a,b,1,*], Xiaojie Shi[a], Yang Zong[a], Yue Wu[a], Jinrun Liu[a], Yi Ouyang[a], Guoxiang Chen[a], Jizhai Cui[a,c], Yongfeng Mei[a,b,c,d,*]

[a] Department of Materials Science, State Key Laboratory of ASIC and Systems, Fudan University, 220 Handan Road, Shanghai 200433, China
[b] Shanghai Frontiers Science Research Base of Intelligent Optoelectronics and Perception, Institute of Optoelectronics, Fudan University, 220 Handan Road, Shanghai 200433, China
[c] Yiwu Research Institute of Fudan University, Chengbei Road, Yiwu, Zhejiang 322000, China
[d] International Institute for Intelligent Nanorobots and Nanosystems, 2005 Songhu Road, Fudan University, Shanghai 200438, China

ARTICLE INFO

Article history:
Received 31 December 2021
Revised 19 February 2022
Accepted 19 March 2022

Keywords:
Magnetic microrobots
Bioinspired motility
Switchable motion modes
Adaptive locomotion
Microfluidic manipulation

ABSTRACT

Mimicry of motile microorganisms offers new concepts and strategies to design and manipulate microrobots. As a representative instance, *Escherichia coli* switches its motility between swimming and tumbling to adapt to surroundings. Inspired by this, we present a tubular microrobot behaving rolling and tumbling motion modes analogous to the motion of *Escherichia coli*, as a result of the anisotropic magnetized status with radially magnetized status at rolling and longitudinally magnetized one at tumbling. The motion behavior of microrobot as rolling or tumbling is determined by the frequency of rotating magnetic field. The threshold frequency for switching is closely related to the amplitude of magnetic field, viscosity of solution and size of microrobot. The net locomotion near substrate comes from the friction and pressure, and the motion switching is due to the magnetized statuses and discrepancy of drag force. The switch from rolling to tumbling endows the microrobot with adaptive locomotion to cross obstacles. Furthermore, microfluidic manipulation through rotational microrobot is achieved based on the local microvortex, which is generated from the hydrodynamic interaction between microrobot and substrate. This manipulation is applied in cargo delivery and release by altering surrounding microfluid via switchable motion modes. This work opens up new possibilities in improving moving ability and extending functions of microrobots through bioinspired motion behaviors.

1. Introduction

Microrobots are artificially fabricated and propelled by different forms of energy to deal with different environments and accomplish designated functionalities [1–5]. Such unique characteristic enables microrobots to be applied in targeted drug delivery [6–8], minimally invasive surgery [9–12], biosensing [13–15], detoxification [16–18], and other biomedical applications [19,20]. It is expected that single microrobot has the ability to accomplish on-demand motion and tasks. To this end, different remote signals [1,3,21,22] and functional modifications [23–26] have been developed to control the motion and design the function of microrobots. However, the limited size of microrobot makes it difficult to realize efficient motility towards complex environment as well as interaction ability with surroundings.

Nature provides plenty of ideal prototypes for microrobots that utilize different strategies to obtain powerful propulsion in microenvironment, together with complex functions. For example, leukocyte, the only motile cell in bloodstream, propels itself efficiently against blood flow to reach the damaged or infected tissues timely. It gets close to the cell-free vessel wall for lower fluid force and performs rolling behavior to move forward as the symmetry in space is broken [27]. Leukocytes-inspired microrollers with efficient translational velocity hold great potential related to the biomedical applications in vasculature [27–29]. Additionally, flagellated *Escherichia coli* cell has also involved its own motility strategy to adapt to the surroundings. The adaptive motion of *Escherichia coli* consists of a sequence of smooth swimming for translational motion and tumbling for rotational motion. The probability of tumbling motion is altered according to the comparison between current and previous chemical environment, leading to a chemotaxis behavior [30–33]. Therefore, new characteristic of *Escherichia coli*

* Corresponding authors at: Department of Materials Science, State Key Laboratory of ASIC and Systems, Fudan University, 220 Handan Road, Shanghai 200433, China.
E-mail addresses: xuborui@fudan.edu.cn (B. Xu), yfm@fudan.edu.cn (Y. Mei).
[1] These authors contributed equally to this work.

https://doi.org/10.1016/j.apmt.2022.101457
2352-9407/

connecting with surroundings is realized based on this specific motion mode switch.

The efficient surface-rolling motion of leukocytes and switchable motion mode of *Escherichia coli* inspire us to design a microrobot with enhanced translational motion and tunable interaction with surroundings. Here, we present an anisotropic magnetized tubular microrobot that can resemble the switchable motion modes of *Escherichia coli*. The microrobot performs rotational motion alike to leukocytes under the remotely controlled rotating magnetic field. As the frequency of rotating magnetic field rises beyond a threshold frequency, the tubular microrobot changes the preferred status from radially magnetized one to longitudinally magnetized one. Therefore, the corresponding motion mode switches from rolling horizontally around the longitudinal axis to tumbling vertically around the radial axis. The threshold frequency is closely correlated with the amplitude of rotating magnetic field, viscosity of solution and size of microrobot. The switchable motion mode occurs due to the competition of drag forces between rolling and tumbling for the anisotropic magnetized tubular microrobot. In addition, the microrobot with the switchable motion mode successfully adapt to rough terrain as the tumbling motion mode makes it easy to get close and cross over vertical obstacles. And the microfluidic manipulation of the microrobot is achieved via altering local microvortex by the motion mode switch, which is attributed to the hydrodynamic interaction between the microrobot and surface boundary. The microvortex alteration is experimentally applied to precisely capture, transport and release microparticles. This work opens up potential use in biomedical and microfluidic applications of microrobots through bioinspired multimodal motion behavior.

2. Results and discussion

2.1. Concept and realization of anisotropic magnetized tubular microrobot

The inspiration of our magnetic microrobots with switchable motion modes comes from the motion alteration of *Escherichia coli* cell. Flagellated *Escherichia coli* involves attribute of chemotaxis to adapt to the surroundings, which is characterized as a sequence of smooth swimming motion punctuated by intermittent tumbling motion (Fig. 1a). The probability of tumbling will be enhanced after perceiving worsening conditions and vice versa. This feature makes *Escherichia coli* prefer to swim smoothly towards attractant and tumble away from repellent [30]. The adaptive motion behavior of *Escherichia coli* gives us a hint that applying modulation of motion modes in microworld can realize complex functions in a confined structure. Thus, we design an anisotropic magnetized microrobot with enhanced translation and manipulation capabilities brought from motion mode switch analogous to *Escherichia coli* (Fig. 1b).

Our microrobot with magnetic components is designed in a tubular architecture and prepared by self-rolled-up nanotechnology (Fig. S1). The fabrication of our tubular microrobot starts from the deposition of Ag, Si, and $Ni_{90}Fe_{10}$ onto a glass substrate. Ni–Fe layer is chosen to offer moving capability under rotating magnetic field, and the layer consisting of Ag and Si provides the internal strain gradient for rolling process. After deposition, the nanomembranes were delaminated and rolled-up into hollow architecture, which was triggered by microdroplet [34]. A representative morphology of the rolled-up microtube with ca. 3 windings is shown in the upper image of Fig. 1c. The length and diameter of the microtube are ca. 125 m and ca. 42 m, respectively. And the enlarged view (lower image of Fig. 1c) indicates that the curly surface of the rolled-up architecture contacts tightly. Besides, the diameter of the microtube is tuned by adjusting the deposition rate of Ni–Fe layer (Fig. 1d) that the increase in deposition rate leads to the microtube with smaller diameter. And also, the length of the microtube is simply tuned by the size of the rectangle pattern for nanomembrane deposition (Fig. S2).

The switch between different motion modes is realized by altering the rotation frequency of magnetic field (Fig. 1e). The microrobot moves in rolling mode below transition frequency $f_{transition}$ and in tumbling mode beyond $f_{transition}$. And microrobot stops moving as the rotation frequency of magnetic field rises above the cut-off frequency $f_{cut\text{-}off}$. It indicates that the tubular microrobot performs switchable motion modes just dependent on appropriate frequency of rotating magnetic field, leading to the on-demand motion manipulation. Snapshots of the optical images in Fig. 1f and g show the microrobot moving in the rolling and tumbling modes, respectively, where the strength of the out-of-plane magnetic field is 3 mT and the viscosity of the solution is 1.2689 mPa•s. At 25 Hz, the microrobot rolls horizontally around the longitudinal axis of the tubular symmetry and moves forward (Fig. 1f and Movie S1). When magnetic field frequency increases to 55 Hz, the microrobot tumbles vertically around the radial axis (Fig. 1g and Movie S2). The translational locomotion of the microrobot is ascribed to the hydrodynamic interaction between the tubular microrobot and the solid surface, which breaks the symmetry of the rotational motion [28]. Besides, the microrobot becomes almost suspended as the field frequency gets higher, which is mainly because that the magnetic moments of the microtube cannot catch up with the quick change of the rotating magnetic field [35,36]. Therefore, the anisotropic magnetized tubular microrobot is proposed to resemble the motion modes of *Escherichia coli*, which are controlled via the frequency of the rotating magnetic field.

2.2. . Motion property affected by environmental and geometric parameters

To quantitatively evaluate the motion behaviors at external stimuli, we firstly investigated the effect of the magnetic field strength on the motion properties of the tubular microrobot. It is well-known that the motion of microrobot is highly dependent on surrounding environment. As for a magnetic microrobot, magnetic field plays a vital role in propulsion. In our experiment. the rotation frequency of the microrobot increases first and then decreases as the frequency of the rotating magnetic field increases (Fig. 2a). Also, there exists a sharp falling slope in rotation frequency, which is attributed to the different motion modes (inset of Fig. 2a). The increase of the rotation frequency corresponds to the motion in rolling mode. Under this circumstance, the microrobot rolls synchronously with the rotating magnetic field. As the magnetic field frequency increases, the microrobot begins to move in tumbling mode, where rotation frequency of the microrobot dramatically falls behind the frequency of the rotating magnetic field. Besides, the rotation frequency drops nearly zero with further increase in the frequency of the rotating magnetic field, indicating the suspended microrobot without effective motion (stop region). Similarly, the velocity of the microrobot increases with rising rotation frequency of the magnetic field, where the microrobot performs rolling motion (Fig. 2b). And then the velocity gets lower due to the motion mode turning into tumbling as highlighted by the dashed circle. It is noteworthy that the velocity of the rotational microrobot drops at the magnetic field frequency close to the transition frequency. The asynchronous rolling behavior of the microrobot at high rotation frequency contributes to this drop of speed [36–38].

We summarized the motion modes of the microrobot related to the frequency and strength of the rotating magnetic field (Fig. 2c). The red points represent the transition frequencies $f_{transition}$ and the yellow points represent the cut-off frequencies $f_{cut\text{-}off}$. By link-

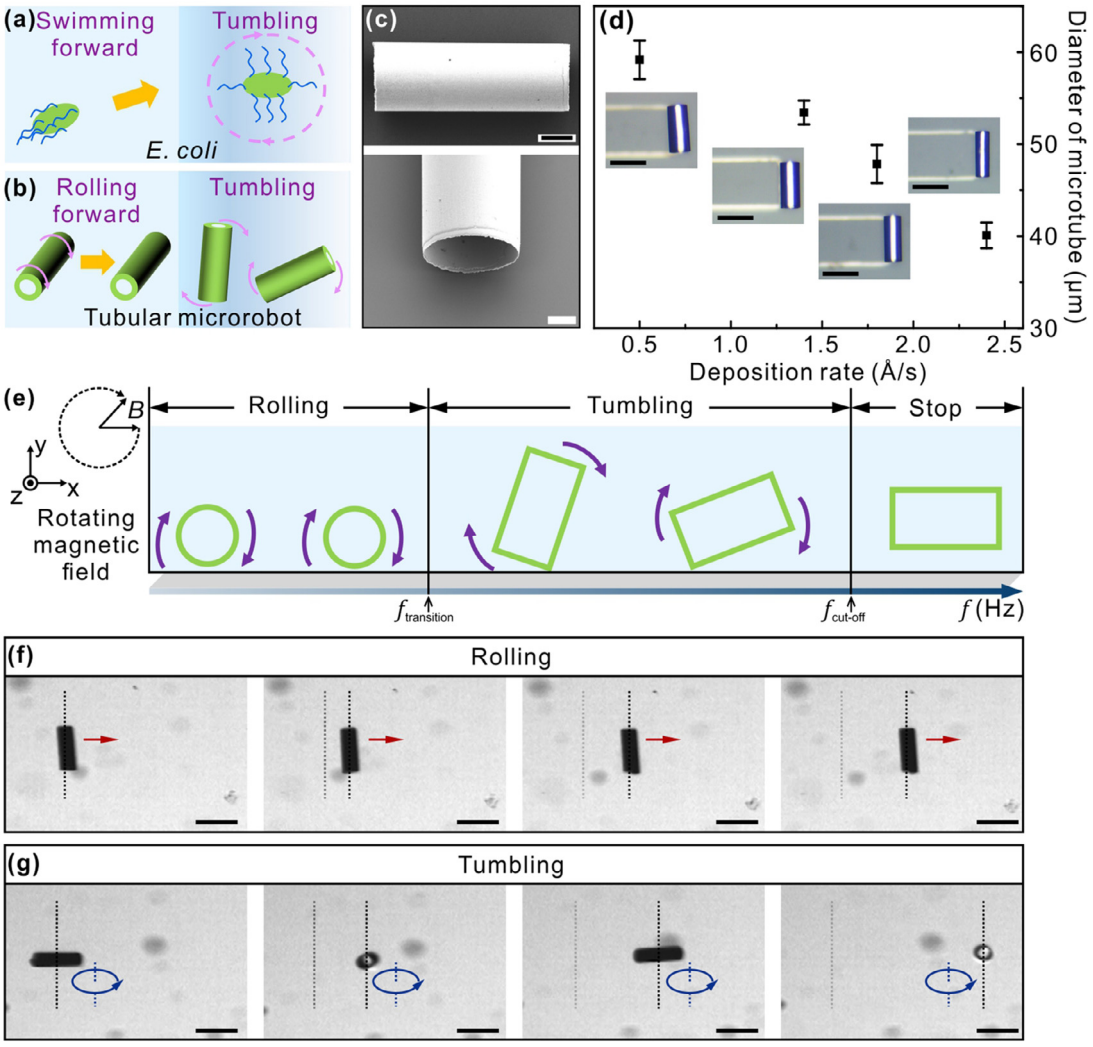

Fig. 1. Concept and realization of anisotropic magnetized microrobot with switchable motion modes. (a) Schematic illustration for the locomotion of *Escherichia coli* with swimming forward and tumbling behavior. (b) Schematic illustration for the tubular microrobot with rolling forward and tumbling behavior. (c) SEM images of the magnetic microtube. Scale bars from upper to lower are 20 μm and 10 μm, respectively. (d) Dependence of the diameter of the rolled-up microtube on the deposition rate of Ni–Fe layer. The insets show the optical morphology of corresponding rolled-up microtubes. Scale bars are 100 μm. (e) Schematic sketch illustrating the motion modes of the tubular microrobot depending on the rotation frequency of in-plane rotating magnetic field. The frequency is divided into three regions according to the motion modes as rolling, tumbling and suspending (stop), where $f_{transition}$ and $f_{cut\text{-}off}$ refers to the transition frequency between different regions. (f) Snapshots for rolling motion of a tubular microrobot under rotating magnetic field of 25 Hz. Red arrows indicate the moving direction. Scale bars are 100 μm. (g) Snapshots for tumbling motion of a tubular microrobot under rotating magnetic field of 55 Hz. Blue arrows indicate the tumbling direction. Scale bars are 100 μm.

ing the red and yellow points with black lines, the phase diagram is divided into three distinct areas referring to rolling (red), tumbling (orange), and stop (blue). It clearly shows that the transition frequency and cut-off frequency increase with the magnetic field strength, which can be attributed to the increasing propulsion force brought from the magnetic torque.

We also investigated the effect of the viscosity on the motion properties of the microrobot when the magnetic field strength is controlled at 3 mT. Here, the dynamic viscosity of the working solution is altered by the concentration of polyvinyl alcohol (PVA) (Fig. S3). Similar with the case in the discussion of the magnetic field, the rotation frequency and velocity of the microrobot increase first as it moves in rolling mode and then decrease for the tumbling motion (Fig. 2d and e). Drop of the velocity exists when the field frequency is close to the transition frequency due to the asynchronous rotational motion. In addition, the transition frequency and cut-off frequency decrease with the increase of the viscosity due to the increasing drag force (Fig. 2f). In a word, the locomotion of the tubular microrobot is modulated by rotating magnetic field frequency, strength and liquid viscosity, implying that the tubular microrobots have the potential to detect the change of viscosity and external magnetic field.

Except from the effect of external stimuli, the motion of the magnetic microrobot is also influenced by its geometric parameters as the structure will affect the magnetic torque and drag force. Here, tubular microrobots in different lengths and diameters were fabricated for investigation (Fig. 3). It can be seen that the microrobots in different geometries all present uniform motion mode switch related to the rotating magnetic field frequency, indicating that this motion mode switch is a general phenomenon in our tubular microrobots. The microrobots in different lengths have slight difference in the rotation frequency and velocity (Fig. 3a and b). Shorter microrobot moving in rolling mode results in a little bit higher velocity, which may come from the hydrodynamic interaction among the microrobot, fluid and substrate. The phase diagram in Fig. 3c shows that the transition frequency decreases slightly with the increase of length. It indicates that longer tubular microrobot tends to facilitate the transition from rolling to tumbling. Be-

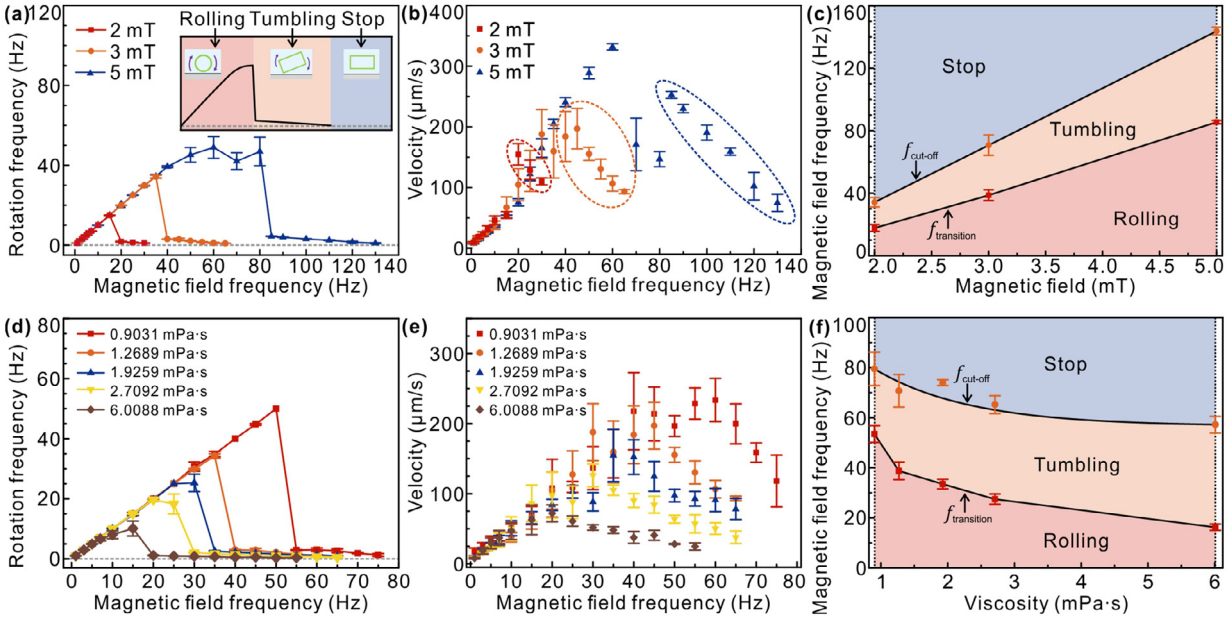

Fig. 2. Motion properties of the tubular microrobot at varied magnetic fields and viscosities. (a) Dependence of rotation frequency of the microrobot on the frequency of different magnetic fields with varied magnetic field strengths. The inset shows the correlation between the motion modes (rolling, tumbling and stop) and the rotation frequency of microrobot. (b) Velocity related to the magnetic field frequency under different magnetic field strengths. Dashed circles refer to the tumbling motion mode. (c) Phase diagram showing the dependence of motion modes on the magnetic field. (d) Dependence of rotation frequency of the microrobot on the frequency of magnetic field in the different viscosity environments. (e) Velocity related to the magnetic field frequency in different viscosity environments. (f) Phase diagram showing the dependence of motion modes on the viscosity.

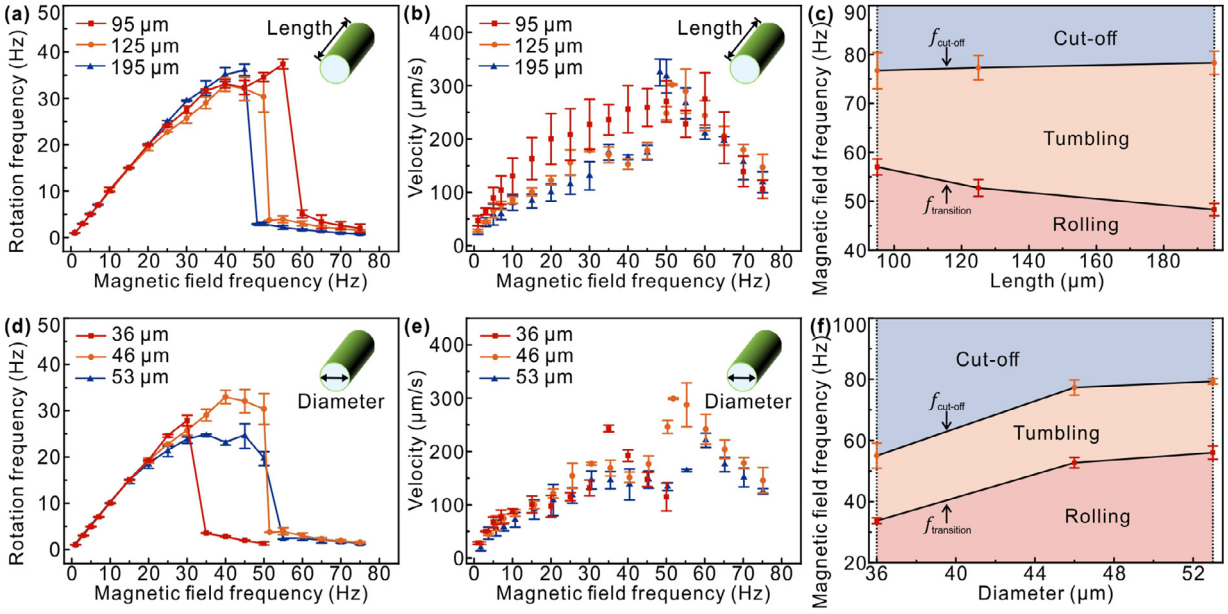

Fig. 3. Motion properties of tubular microrobots with different geometries. (a) Dependence of rotation frequency of the microrobot with different lengths (diameter, ca. 47 μm) on the frequency of magnetic field. (b) Velocity related to the length of microrobot. (c) Phase diagram showing the dependence of motion modes on the length. (d) Dependence of rotation frequency of the microrobot with different diameters (length, ca. 125 μm) on the frequency of magnetic field. (e) Velocity related to the diameter of microrobot. (f) Phase diagram showing the dependence of motion modes on the diameter.

sides, there is no obvious difference found in the cut-off frequency. With respect to the diameter of the tubular microrobot, an upward trend of transition and cut-off frequencies with the increase of diameter is observed (Fig. 3d–f).

2.3. Mechanisms of motion mode switch

To figure out the reason of net locomotion near a substrate, we investigated the total force along the horizontal direction (x direction) through simulation. The friction and pressure at different point on the microtube surface, which is signed by central angle is calculated in Fig. 4a. It can be seen that obvious pressure and friction generated around 90°, corresponding to the bottom point of microtube. It also reflects that the pressure hinders the microtube to move forward, while the friction provides the propulsion force. Therefore, the translational motion of rolling microtube can be attributed to the friction generated from the hydrodynamic interaction between microtube and bottom substrate. To better un-

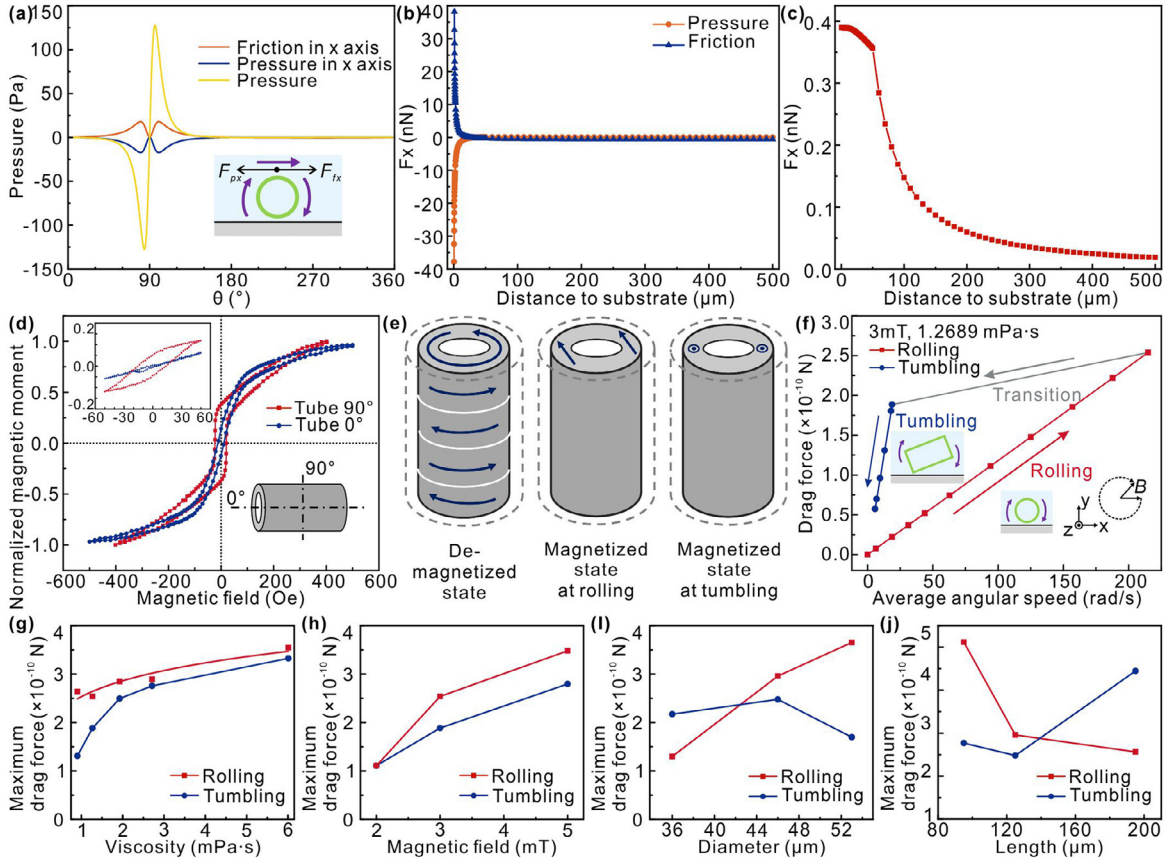

Fig. 4. Mechanism of self-propulsion and motion mode switch due to fluid friction, magnetization state and drag force. (a) The fluid friction and pressure applied on the rolling microrobot related to the central angle. Inset depicts the model that rolling microrobot above the surface generates translational motion due to the competition between friction (F_{fx}) and pressure (F_{px}). (b) Dependence of friction and pressure in x axis with the distance to substrate. (c) Total force in x axis as a function of the distance to substrate. (d) Magnetic hysteresis loops of the ferromagnetic microtube. Red curve illustrates the hysteresis curve perpendicular (90°) to the longitudinal axis of the tubular symmetry, and blue curve illustrates the hysteresis curve parallel (0°) to the longitudinal axis of the tubular symmetry. The inset in the bottom right corner shows the definition of measured degree. The inset in the top left corner shows the hysteresis loops up to the magnetic strength of 5 mT. (e) Magnetization states of the tubular microrobot under circumstances including demagnetized, rolling, and tumbling state. (f) Calculated drag force of the microrobot. The viscosity and magnetic field amplitude are set as 1.2689 mPa•s and 3 mT, respectively. The insets schematically show the rolling and tumbling motion under the rotating magnetic field. (g) Calculated maximum drag force at rolling and tumbling modes in the fluid with different viscosities. (h) Calculated maximum drag force at rolling and tumbling modes under varied magnetic field strength. (i) Calculated maximum drag force at rolling and tumbling modes for the microrobots with different diameters (length, ca. 125 μm). (j) Calculated maximum drag force at rolling and tumbling modes for the microrobots with different lengths (diameter, ca. 47 μm).

derstand the role of distance between microtube and substrate surface, Fig. 4b and c present the pressure, friction and total force in x direction related to the distance. It reveals that both pressure and force dramatically decrease with increasing distance, which leads to the decrease of total force. As the distance increases further, the friction and pressure could approach to zero (Fig. S4). And without a substrate, the microtube only rotates without net translation, together with a different motion mode switch manner (Fig. S5). The simulation results indicate that the effect of total force including friction and drag force makes the rolling microrobot with symmetrical structure obtain net locomotion in the low Reynolds (Re) number fluid.

In order to reveal the reason for the rolling and tumbling motion of the microrobot, we measured the magnetic hysteresis loop of the tubular microrobot in longitudinal axis (0°) and radial direction (90°) (Fig. 4d). The hysteresis loop measured along the radial direction shows a little larger remanence and coercive field than that along the longitudinal direction which is verified by the hysteresis loops up to the strength of 5 mT (inset in the top left corner of Fig. 4d), indicating circular magnetic easy axis of the magnetic microtube, which is similar to the previous work [39]. Based on the magnetic hysteresis loops, the magnetization of tubular microrobot is proposed to be circular configuration at demagnetized state (left image of Fig. 4e), which was also reported in other tubular magnetic architectures [39,40]. The permalloy ($Ni_{90}Fe_{10}$) exhibits a negative magnetostriction constant [41] that imparts strain-induced anisotropy to the rolled-up microtube. As the frequency of rotating magnetic field changes, the tubular microrobot exhibits anisotropic magnetized status. At low rotation frequency, the circular magnetization of the tubular microrobot tends to be easily aligned to the direction of the rotating magnetic field, resulting in effective magnetic moments aligning to radial axis (middle image of Fig. 4e), namely radially magnetized state. Therefore, the magnetic torque provided by the rotating magnetic field drives the tubular microrobot to rotate horizontally around its longitudinal axis, which leads to the rolling behavior. However, after the motion of tubular microrobot enters into asynchronous region, the hydrodynamic interaction between microrobot and fluid becomes significant and the microrobot switches into tumbling motion. Thereby, the magnetized state changes to longitudinal one and the effective magnetic moments parallel to the longitudinal axis of the microtube (right image of Fig. 4e) enable the continuous tumbling motion driven by the rotating magnetic field. Similar rolling and tumbling motion are also observed in a peanut-shaped micromotor with permanent magnetic moment vertical to the long axis of peanut colloid under the control of rotating magnetic field [42].

They also presented an interesting wobbling motion using a conical rotating magnetic field. Since the tubular microrobot can be radially magnetized under rotating magnetic field, similar as the magnetization direction of peanut colloid motor, it is believed that the tubular microrobot could also display stable wobbling motion under a conical rotating magnetic field which needs further study.

Furthermore, we estimated the drag force applied on the microrobot in the two motion modes to analyze the reason for the orientation of the tubular microrobot. In low Re number fluid with neglected inertial force, rotating magnetic field supplies the power for the motion of microrobot with considerable dissipated energy. And the microrobot exposed to rotating magnetic field is subjected to a balanced drag force. Based on this consideration, the drag force applied on the microrobot in rolling and tumbling motion was calculated as shown in Fig. 4f for a representative instance. In the rolling region, the drag force increases linearly with the increase of angular speed and reaches a maximum value of ca. 2.5×10^{-10} N (red arrow in Fig. 4f). In the meantime, in the tumbling region, the drag force decreases with the decrease of angular speed, showing a maximum drag force of ca. 1.9×10^{-10} N (blue arrow in Fig. 4f). The difference of the maximum drag force exerted on the microrobot in rolling and tumbling motion may drive the orientation of microrobot from rolling to tumbling as the microrobot's motion gets into asynchronous region.

The maximum drag forces in rolling (F_{rm}) and tumbling (F_{tm}) motion are compared and analyzed related to different environmental and geometric parameters (Fig. S6). As the viscosity grows, the maximum drag force increases accordingly both for rolling and tumbling modes (Fig. 4g), and the force for rolling is higher than the one for tumbling. Additionally, the difference of the maximum drag forces between rolling and tumbling modes, defined as $\Delta F_m = F_{rm} - F_{tm}$, reflects the difficulty of motion mode transition from rolling to tumbling. A lower difference in force requires a lower angular speed for transition. Thus, a lower transition frequency $f_{\text{transition}}$ is obtained in high viscosity environment. In contrast, the force difference ΔF_m tends to increase with rising magnetic field strength (Fig. 4h), leading to a higher transition frequency $f_{\text{transition}}$. Regarding the case in geometric parameters, discrepancy of maximum drag forces ΔF_m tends to grow with a microrobot in larger diameter and smaller length (Fig. 4i and j). As a result, higher transition frequency $f_{\text{transition}}$ is needed for a plump microrobot. Although the microrobot together with low Re fluid is a complicated energy-dissipated system, the drag force is crucial to the switchable behavior of the motion and it is clarified that the discrepancy of drag force at different motion modes contributes to the orientation of the tubular microrobots. In previous literature, the tumbling motion of a slender body nanopropeller is observed at low Re numbers and is switched to propulsion motion at high frequency. The motion switch is mainly ascribed to the effect of thermal fluctuation [43]. However, in our system, the effect of thermal fluctuation on the microscale tubular robot can be neglected, resulting in a different moving manner.

2.4. . Adaptive locomotion

Similar with the *Escherichia coli* that switches its motion from swimming to tumbling to adapt to the surrounding after stimuli, the tubular microrobot with the switchable motion modes from rolling to tumbling shows enhanced adaptive ability to overcome vertical obstacles (Fig. 5a). The adaptive ability was tested using an artificial obstacle with a height of ca. 100 μm (Fig. 5b and Movie S3). At rolling motion mode, the tubular microrobot is hindered by the obstacle. When increasing the rotation frequency of magnetic field, the microrobot transforms motion behavior into tumbling mode and thereby crosses the obstacle successfully. As the tubular microrobot switches into tumbling motion near an obstacle, the place of upper half of the tube could mechanically touch the edge of obstacle. With the friction and drag force, the tubular microrobot crosses the obstacle and obtains net locomotion in the fluid. Hence, we experimentally demonstrate the ability in crossing obstacle using the tubular microrobot with switchable motion modes under the remote control of magnetic field.

It is noticed that there exists a certain distance between the rolling microrobot and the wall as the microrobot stops moving forward. This phenomenon reflects that the resistance for translational moving comes from hydrodynamic interaction between microrobot and wall rather than solid contact. A 2D model with finite element method (FEM) was carried out to distinguish the hydrodynamic difference in different moving manners (Fig. S7). Here, the rotation frequency in rolling manner was set as 50 Hz, while the one in tumbling manner was set as 2 Hz according to the experiment results. The fluid field around the rotational microrobot is much stronger than the one around the tumbling microrobot (Fig. 5c). In the meantime, the confinement of wall leads to a localized area of high fluid pressure applied on the microrobot, as the rotational microrobot suffers from higher pressure compared with the tumbling one (Fig. 5d). Therefore, the total force applied on the microrobot is dependent on the moving manners of the microrobot and the distance between microrobot and wall (Figs. 5e and S8). We focus on the force in x direction, which denotes the drag force applied on the microrobot directly influencing its motion. It is observed that the drag force applied on rotational microrobot increases with smaller distance from the wall, and it increases dramatically as the distance reaches less than 50 μm (Fig. 5e). But the force applied on a tumbling microrobot is dependent on its current tumbling states (Fig. S9). Still, it can be concluded that the drag force applied on a rotational microrobot is larger than a tumbling one under the same rotation frequency. Besides, the drag force decreases as the rotation frequency gets lower. Considering that the tumbling motion appears in the asynchronous region where the rotation frequency falls far behind the magnetic field rotation frequency, the drag force becomes smaller significantly as the motion mode changes from rolling into tumbling. Therefore, the microrobot can move close to and overcome the vertical barrier with proper alteration in magnetic field rotation frequency. In the biomedical area, such as in vessel or intestinal tract with rough terrain which will obstruct the motion of microrobots, this kind of magnetic microrobots with switchable motion modes has significant advantage in negotiating the unstructured surfaces with complex terrains.

2.4. Microfluidic manipulation

In the fluid environment, hydrodynamic interaction around a rotating object results in local microvortex. The potential of microrobot is expanded in microfluidic field taking advantage of induced microvortex [44]. Interestingly, benefiting from the switchable motion modes, the tubular microrobots can tune the local microvortex sharply in a short period (Fig. 6a). In our experiment, polystyrene (PS) microspheres with average diameter of 5 μm were dispersed in the working solution to trace the microvortex around the microrobot. It is clearly shown that many particles moving around the microrobots and confined in a limited area (Movies S4 and S5). Then we utilized a grayscale background subtraction analysis to clarify the particles that move together with the microrobot (second row of Fig. 6a). The white spots depict the particles that doesn't present in their original location, so they are moving together with the microrobots. Therefore, the edge of the spot cluster, as outlined by red dashed curves, represents the distribution of local microvortex. It can be found that the area of microvortex induced by microrobot in rolling mode increases with the rising

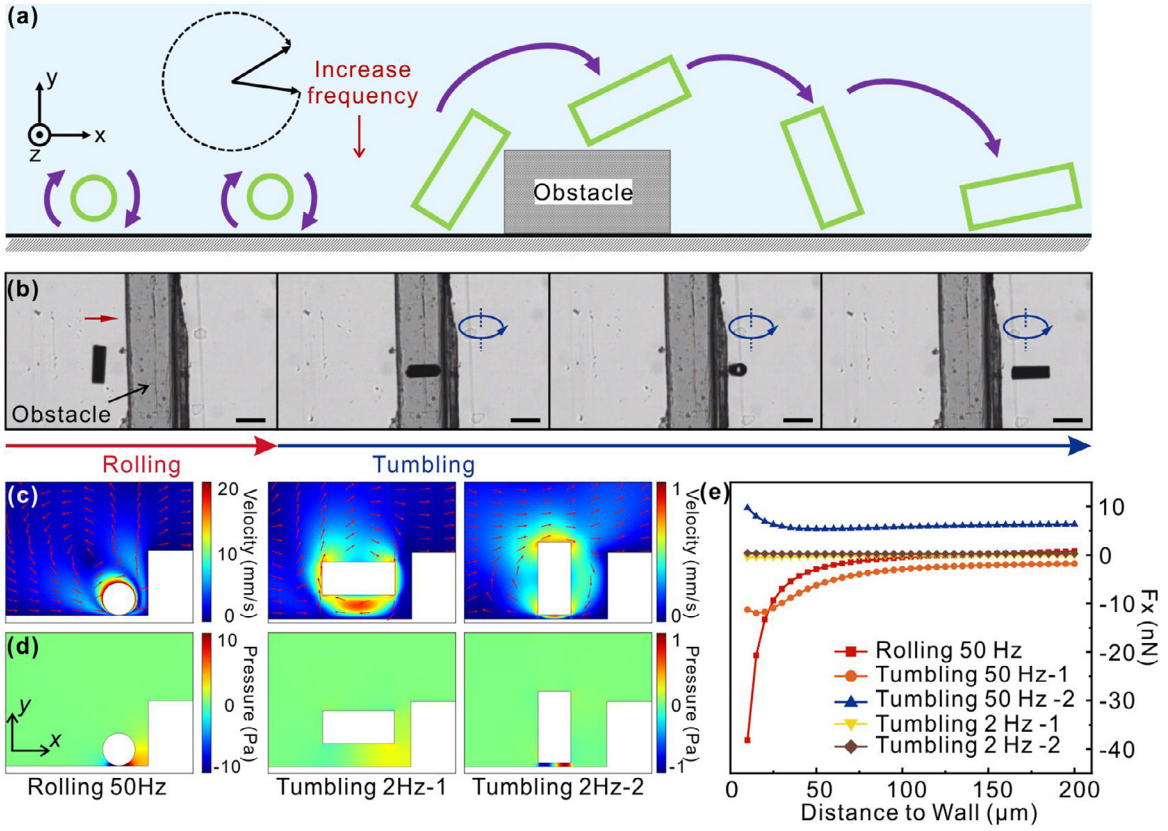

Fig. 5. Adaptive locomotion for obstacle-crossing based on the motion mode switch. (a) Schematic sketch illustrating the motion design for crossing obstacle. (b) Sequential optical images of the microrobot crossing the obstacle with the height of ca. 100 μm. Scale bars are 100 μm. (c) Fluid field generated by the microrobot in rolling (50 Hz) and tumbling (2 Hz) manners. The distance between microrobot and wall is 20 μm. Red arrows indicate the fluid flow direction. (d) Pressure generated by the microrobot in rolling (50 Hz) and tumbling (2 Hz) manners. (e) The force in *x* direction acting on the microrobot in rolling and tumbling manners related to the distance from the wall.

rotation frequency. And it is much larger than the one induced by microrobot in tumbling mode.

Furthermore, we performed finite element method (FEM) to simulate the fluid flow distribution around the rolling and tumbling microrobot (third row in Fig. 6a). It presents similar fluid flow as the experimental results, reflecting that the microvortex is ascribed to the hydrodynamic interaction between rotating microrobot and solid glass substrate. White dashed curve in simulation results is the contour where relative horizontal velocity of fluid equals zero, which means the fluid moving together with microrobot at the same speed. This can be regarded as the edge of the vortex. To further elucidate the vortex area related to the motion of microrobot, Fig. 6b gives normalized vortex length of the microrobots in different motion behaviors. The vortex length is defined as the horizontal distance between the edge of vortex and the center of the microrobot. It is concluded that both experimental and simulation results have the same tendency that the vortex area rises with faster rotation speed, and it becomes much smaller as the microrobot's motion changes from rolling into tumbling mode.

With tunable vortex area, the tubular microrobot is designed to capture, transport and release microparticles. As sketched in Fig. 6c, the microparticle is captured by the vortex generated by the rolling motion, followed by translating along with the rotational microrobot. And then, the microparticle is released as the motion mode of the microrobot is switched into tumbling one. Fig. 6d evidently shows the processes of capturing and transporting microparticle by the tubular microrobot (Movie S6). The PS microsphere is captured around one end of tubular structure by the rotational microrobot, and travels a distance as the microrobot rolls forward. It is found that the velocity of the trapped microparticle declines exponentially with the increase of the distance to the center of microrobot (Fig. S10). When changing the motion mode of the microrobot from rolling to tumbling via simply adjusting the rotation frequency of magnetic field, the microparticle is left behind by the tumbling microrobot (Fig. 6e and Movie S7). Therefore, we demonstrate that the tubular microrobot with switchable motion modes has the capability in versatile transport and release applications through altering microvortex. It is also noteworthy that other function can be extended by the switchable motion modes and the hollow structure of the rolled-up microrobot also can be filled with drug gels for cargo transporting.

3. Conclusion

In conclusion, we propose a kind of anisotropic magnetized tubular microrobots, which is fabricated using nanomembrane deposition methods and assembled via microdroplet-assisted lift-off method. The rolled-up microrobot immersed in viscous fluid and under control of rotating magnetic field exhibits anisotropic magnetized status and shows switchable motion modes between rolling and tumbling, subject to a threshold frequency of out-of-plane rotating magnetic field. The amplitude of magnetic field, viscosity of solution and size of tubular microrobot play important roles in the motion mode switch properties. Rolling motion is mainly ascribed to the circular magnetic easy axis of the tubular structures and the net locomotion obtained by the rolling motion of the tubular microrobot can be ascribed to the competition between friction and pressure from the fluid with the existence of substrate. And the motion switching from rolling to tumbling is closely related to the discrepancy of drag force exerted on the mi-

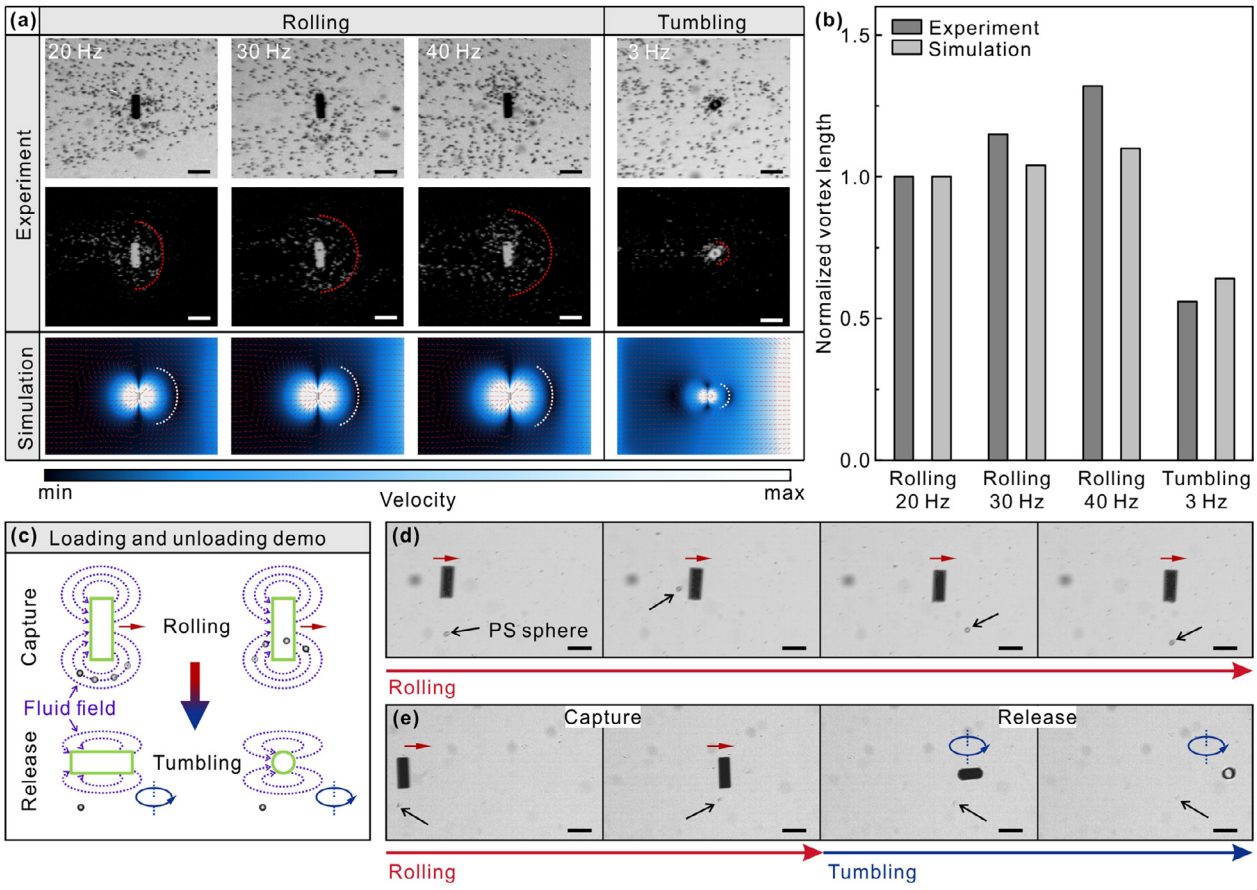

Fig. 6. Microfluidic manipulation in cargo transporting and releasing due to the tunable local microvortex of tubular microrobots with switchable motion modes. (a) Local microvortex in different motion modes and rotation speed in experiment and simulation. First row depicts the microrobot moves in rolling and tumbling modes in the solution containing PS particles for vortex tracing. Second row depicts the grayscale background subtraction images to illustrate the particles that move in the solution with microrobot. Red dashed curves depict the edge of particle moving area. White dashed curves in Simulation images depict the contour where relative fluid velocity in horizontal direction equals zero. Scale bars are 100 μm. (b) Comparison of the area of microvortices between simulation and experiment. The vortex length refers to the horizontal distance between the edge of the vortex area to the center of microrobot. (c) Schematically showing the processes of capturing and releasing particles via the microvortex induced by different motion modes. (d) Sequential optical images of the tubular microrobot capturing a PS microsphere at rolling motion mode. Scale bars are 100 μm. (e) Sequential optical images of the tubular microrobot capturing and releasing microparticle via rolling and tumbling motion modes. Scale bars are 100 μm.

crorobot at rolling and tumbling. The anisotropic magnetized microrobot with motion switch behavior has the adaptive capability in crossing vertical obstacles on the surface due to the decreased drag force. Moreover, the rolling and tumbling motion modes generate different local microvortices due to the hydrodynamic interaction between microrobot and solid surface, which is further confirmed by numerical simulation. Using the microrobot with switchable motion modes, the microfluidic manipulation through tunable microvortex is applied in capturing, transporting and releasing microparticles. We expect that this kind of tubular microrobots opens up new possibilities serving as micropump and microroller in the manipulation of microfluid. And the tubular microrobot can act as drug delivery microtool via filling the hollow cavity with drug loaded gels. This work may also inspire the research focusing on the switchable motion modes of microrobots and functionality extension induced by different motion modes.

4. Materials and methods

4.1. Fabrication of tubular microrobot

The fabrication method is reported in our previous work as illustrated in Fig. S1 [34]. Glass slide covered by a shadow mask with rectangular pores was used as the substrate. Silver (Ag), silicon (Si) and permalloy ($Ni_{90}Fe_{10}$) were deposited successively onto the substrate by electron beam evaporator (TSV70, Tenstar). The deposition thickness was tuned as 60 nm for each layer. And the deposition speeds of Ag, Si and $Ni_{90}Fe_{10}$ layers were set as 0.7–2.0 Å s^{-1}, 0.5–1.5 Å s^{-1} and 0.3–3.0 Å s^{-1}, respectively. After deposition, the 2D nanomembranes were rolled-up into tubular microstructures via self-delamination, which was triggered by one microdroplet of alcohol through a tiny capillary tube with a diameter of several microns.

4.2. Material characterization

The optical morphology of the microtube was conducted on the microscope (Olympus BX51). The high-resolution morphologies were observed by scanning electron microscope (SEM, Zeiss Sigma 300) at 5 kV. The superconducting quantum interference device (SQUID) magnetometer (Quantum Design MPMS) was used to measure the hysteresis loops of the magnetic microtube radially and longitudinally.

4.3. Motion investigation

The working solution for the motion investigation of the microrobots was prepared using water solution containing different concentrations of polyvinyl alcohol (PVA) (0, 1.0, 2.0, 3.0 and 5.0 wt.%).

The surfactant as sodium dodecyl sulfate (SDS) (0.5 wt.%) was also added into the solution.

The working solution was added onto a clean glass substrate. Then, the tubular microrobot was transferred into the working solution. The motion of the microrobots was controlled by a rotating magnetic field, which was generated by orthogonally 3-dimentional couples of Helmholtz coils. And the motion process was recorded by high speed CCD camera connected with an optical microscope (Olympus IX73). The velocity and rotation frequency of the microrobots were analyzed via ImageJ software. The grayscale background subtraction analysis of spreading particles was carried out by Adobe Photoshop.

4.4. Drag force calculation

The drag force exerted on the microrobot is proportional to the instantaneous velocity of fluid if we focus on the rotational motion of the tubular microrobot regardless of the hydrodynamic interaction between the microrobot and the surface. For simple assumption, the absolute value of drag force exerted on the tubular microrobot with characteristic size L can be expressed as [45,46]:

$$F = kL\eta v \tag{1}$$

where k represents the friction coefficient, η denotes the dynamic viscosity of fluid, and v denotes the instantaneous velocity by virtue of rotational motion. It is noted that the instantaneous velocity can be described as $v = wR$ at the surface of the rotational microrobot, where w and R denote the instantaneous angular velocity and the distance to the microrobot's center, respectively.

Herein, we simplify the tubular microrobot as a closed cylinder for the estimation of drag force. Considering the anisotropy of the friction coefficient of a closed cylinder, the friction coefficients of k_r at rolling and k_t at tumbling for a tubular microrobot with length (L) and diameter (D) can be described as [47–50].

$$k_r = \pi\left(\frac{D}{L}\right)^2 \tag{2}$$

$$k_t = \frac{\pi}{3}\left(\ln\left(\frac{2L}{D}\right) - 1.45 + 7.5\left(\frac{1}{\ln\left(\frac{2L}{D}\right)} - 0.27\right)^2\right) \tag{3}$$

Then, the drag force at rolling motion (F_r) and tumbling motion (F_t) can be estimated as:

$$F_r = \frac{1}{2}k_r LD\eta\omega \tag{4}$$

$$F_t = \frac{1}{2}k_t L^2\eta\omega \tag{5}$$

Using Eqs. (2)–(5), the drag force was calculated based on the average angular speed of the tubular microrobot.

4.5. Fluid simulation

The simulation of fluid flow during microrobot's motion was conducted on COMSOL Multiphysics. To find out the friction and pressure applied on a microrobot near a surface, 2D model with laminar flow interface was applied. Here, the rotating frequency was set as 50 Hz. The translational velocity was zero as we focused on the force generation due to the rotating motion. The pressure and friction were plotted and integrated by outputting the data of pressure and viscous force in COMSOL. And total force came from the data of total traction.

To analyze the hydrodynamic interaction between microrobot and a vertical wall, 2D model with laminar flow interface was applied (Fig. S7). The distance between microrobot and bottom substrate was set as 400 nm according to the calculated estimation (Details can be found in supplementary information) [51,52]. The translational velocity of microrobot was set as zero, as we assume that the translational motion of microrobot is hindered by the wall. The velocity of the microrobot edge was determined by the angular speed and the distance from the microrobot center. To obtain the force acting on the microrobot, the x or y component of the stress on the microrobot edge was firstly integrated and then times the microrobot length in z direction. The microrobot length in z direction was estimated as the tube length when moving in rolling manner, and the tube diameter when moving in tumbling manner.

As for the simulation of fluid flow surrounding the tubular microrobot in 3D space, the laminar flow interface of rotating machinery was chosen. Tubular microrobot with length in 110 μm and diameter in 50 μm was placed at the bottom of fluid area. And the distance between microrobot and bottom substrate was set as 10 μm to obtain better convergence. For microrobots in rolling and tumbling behavior, the velocity of inlet was set as the translational velocity and the rotation frequency of rotating domain was set according to the angular speed of microrobot, which are obtained from the experiments. Using Frozen Rotor Study, we simulated the fluid distribution under the stationary rotation of microrobot.

Declaration of Competing Interest

The authors declare that they have no known competing financial interests or personal relationships that could have appeared to influence the work reported in this paper.

CRediT authorship contribution statement

Guanghui Yan: Investigation, Methodology, Formal analysis, Conceptualization, Writing – original draft. **Borui Xu:** Methodology, Formal analysis, Conceptualization, Writing – review & editing. **Xiaojie Shi:** Formal analysis, Methodology, Writing – review & editing. **Yang Zong:** Formal analysis, Methodology, Writing – review & editing. **Yue Wu:** Formal analysis, Methodology, Writing – review & editing. **Jinrun Liu:** Investigation, Formal analysis, Writing – review & editing. **Yi Ouyang:** Formal analysis, Writing – review & editing. **Guoxiang Chen:** Formal analysis, Methodology, Writing – review & editing. **Jizhai Cui:** Supervision, Formal analysis, Writing – review & editing. **Yongfeng Mei:** Supervision, Conceptualization, Formal analysis, Project administration, Writing – review & editing.

Acknowledgements

The authors acknowledged C. Liu and Z. Zhao for the help in taking SEM images. This work was supported by the National Natural Science Foundation of China (nos. 51961145108, 61975035, and 62005050); the Project funded by China Postdoctoral Science Foundation (no. 2021M700786); and the Program of Shanghai Academic Research Leader (no. 19XD1400600).

Supplementary materials

Supplementary material associated with this article can be found, in the online version, at doi:10.1016/j.apmt.2022.101457.

References

[1] S. Palagi, A.G. Mark, S.Y. Reigh, et al., Structured light enables biomimetic swimming and versatile locomotion of photoresponsive soft microrobots, Nat. Mater. 15 (2016) 647–653.

[2] T. Li, J. Li, H. Zhang, et al., Magnetically Propelled Fish-Like Nanoswimmers, Small 12 (2016) 6098–6105.
[3] W. Wang, L.A. Castro, M. Hoyos, et al., Autonomous motion of metallic microrods propelled by ultrasound, ACS Nano 6 (2012) 6122–6132.
[4] W. Gao, K.M. Manesh, J. Hua, et al., Hybrid nanomotor: a catalytically/magnetically powered adaptive nanowire swimmer, Small 7 (2011) 2047–2051.
[5] H. Zhou, C.C. Mayorga-Martinez, S. Pane, et al., Magnetically Driven Micro and Nanorobots, Chem. Rev. 121 (2021) 4999–5041.
[6] X.Z. Chen, M. Hoop, N. Shamsudhin, et al., Hybrid Magnetoelectric Nanowires for Nanorobotic Applications: Fabrication, Magnetoelectric Coupling, and Magnetically Assisted In Vitro Targeted Drug Delivery, Adv. Mater. 29 (2017) 1605458.
[7] Z. Hosseinidoust, B. Mostaghaci, O. Yasa, et al., Bioengineered and biohybrid bacteria-based systems for drug delivery, Adv. Drug Deliv. Rev. 106 (2016) 27–44.
[8] W. Gao, D. Kagan, O.S. Pak, et al., Cargo-towing fuel-free magnetic nanoswimmers for targeted drug delivery, Small 8 (2012) 460–467.
[9] B.J. Nelson, I.K. Kaliakatsos, J.J. Abbott, Microrobots for Minimally Invasive Medicine, Annu. Rev. Biomed. Eng. 12 (2010) 55–85.
[10] S.K. Srivastava, M. Medina-Sanchez, B. Koch, et al., Degradable Magnetic Composites for Minimally Invasive Interventions: Device Fabrication, Targeted Drug Delivery, and Cytotoxicity Tests, Adv. Mater. 28 (2016) 832–837.
[11] G. Chatzipirpiridis, O. Ergeneman, J. Pokki, et al., Electroforming of implantable tubular magnetic microrobots for wireless ophthalmologic applications, Adv. Healthc. Mater. 4 (2015) 209–214.
[12] E. Diller, M. Sitti, Three-Dimensional Programmable Assembly by Untethered Magnetic Robotic Micro-Grippers, Adv. Funct. Mater. 24 (2014) 4397–4404.
[13] J. Wang, Self-propelled affinity biosensors: Moving the receptor around the sample, Biosens. Bioelectron. 76 (2016) 234–242.
[14] X. Yu, Y. Li, J. Wu, et al., Motor-based autonomous microsensor for motion and counting immunoassay of cancer biomarker, Anal. Chem. 86 (2014) 4501–4507.
[15] S. Balasubramanian, D. Kagan, C.-M.J. Hu, et al., Micromachine-enabled capture and isolation of cancer cells in complex media, Angew. Chem. Int. Ed. 50 (2011) 4161–4164.
[16] W. Zhu, J. Li, Y.J. Leong, et al., 3D-Printed Artificial Microfish, Adv. Mater. 27 (2015) 4411–4417.
[17] Z. Wu, T. Li, W. Gao, et al., Cell-Membrane-Coated Synthetic Nanomotors for Effective Biodetoxification, Adv. Funct. Mater. 25 (2015) 3881–3887.
[18] Z. Wu, J. Li, B.E.-F. de Ávila, et al., Water-Powered Cell-Mimicking Janus Micromotor, Adv. Funct. Mater. 25 (2015) 7497–7501.
[19] X. Yan, Q. Zhou, M. Vincent, et al., Multifunctional biohybrid magnetite microrobots for imaging-guided therapy, Sci. Robot. 2 (2017) eaaq1155.
[20] Z.W. Tay, P. Chandrasekharan, A. Chiu-Lam, et al., Magnetic Particle Imaging-Guided Heating in Vivo Using Gradient Fields for Arbitrary Localization of Magnetic Hyperthermia Therapy, ACS Nano 12 (2018) 3699–3713.
[21] J. Li, T. Li, T. Xu, et al., Magneto-Acoustic Hybrid Nanomotor, Nano Lett. 15 (2015) 4814–4821.
[22] R. Dreyfus, J. Baudry, M.L. Roper, et al., Microscopic artificial swimmer, Nature 437 (2005) 862–865.
[23] J. Li, F. Ji, D.H.L. Ng, et al., Bioinspired Pt-free molecularly imprinted hydrogel-based magnetic Janus micromotors for temperature-responsive recognition and adsorption of erythromycin in water, Chem. Eng. J. 369 (2019) 611–620.
[24] J. Liu, J. Li, G. Wang, et al., Bioinspired zeolitic imidazolate framework (ZIF-8) magnetic micromotors for highly efficient removal of organic pollutants from water, J. Colloid Interface Sci. 555 (2019) 234–244.
[25] S. Park, G. Yossifon, Micromotor-Based Biosensing Using Directed Transport of Functionalized Beads, ACS Sens. 5 (2020) 936–942.
[26] B. Jurado-Sánchez, M. Pacheco, J. Rojo, et al., Magnetocatalytic Graphene Quantum Dots Janus Micromotors for Bacterial Endotoxin Detection, Angew. Chem. Int. Ed. 56 (2017) 6957–6961.
[27] Y. Alapan, U. Bozuyuk, P. Erkoc, et al., Multifunctional surface microrollers for targeted cargo delivery in physiological blood flow, Sci. Robot. 5 (2020) eaba5726.
[28] U. Bozuyuk, Y. Alapan, A. Aghakhani, et al., Shape anisotropy-governed locomotion of surface microrollers on vessel-like microtopographies against physiological flows, Proc. Natl. Acad. Sci. USA 118 (2021) e2022090118.
[29] T. Yang, A. Tomaka, TO. Tasci, et al., Microwheels on microroads: Enhanced translation on topographic surfaces, Sci. Robot. 4 (2019) eaaw9525.
[30] D.J. Webre, P.M. Wolanin, J.B. Stock, Bacterial chemotaxis, Curr. Biol. 13 (2003) R47–R49.
[31] S. Palagi, P. Fischer, Bioinspired microrobots, Nat. Rev. Mater. 3 (2018) 113–124.
[32] M.D. Baker, P.M. Wolanin, J.B. Stock, Signal transduction in bacterial chemotaxis, BioEssays 28 (2005) 9–22.
[33] G.H. Wadhams, J.P. Armitage, Making sense of it all: bacterial chemotaxis, Nature 5 (2004) 1024–1037.
[34] B. Xu, X. Zhang, Z. Tian, et al., Microdroplet-guided intercalation and deterministic delamination towards intelligent rolling origami, Nat. Commun. 10 (2019) 1–10 5019.
[35] Y. Mei, G. Huang, A.A. Solovev, et al., Versatile Approach for Integrative and Functionalized Tubes by Strain Engineering of Nanomembranes on Polymers, Adv. Mater. 20 (2008) 4085–4090.
[36] A. Ranzoni, X.J. Janssen, M. Ovsyanko, et al., Magnetically controlled rotation and torque of uniaxial microactuators for lab-on-a-chip applications, Lab Chip 10 (2010) 179–188.
[37] L. Zhang, J.J. Abbott, L. Dong, et al., Characterizing the swimming properties of artificial bacterial flagella, Nano Lett. 9 (2009) 3663–3667.
[38] L. Zhang, J.J. Abbott, L. Dong, et al., Artificial bacterial flagella: fabrication and magnetic control, Appl. Phys. Lett. 94 (2009) 064107.
[39] D. Karnaushenko, D.D. Karnaushenko, D. Makarov, et al., Self-Assembled On-Chip-Integrated Giant Magneto-Impedance Sensorics, Adv. Mater. 27 (2015) 6582–6589.
[40] R. Streubel, J. Lee, D. Makarov, et al., Magnetic microstructure of rolled-up single-layer ferromagnetic nanomembranes, Adv. Mater. 26 (2014) 316–323.
[41] L.W. McKeehan, P.P. Cioffi, Magnetostriction in permalloy, Phys. Rev. 28 (1926) 146–158.
[42] Z. Lin, X. Fan, M. Sun, et al., Magnetically Actuated Peanut Colloid Motors for Cell Manipulation and Patterning, ACS Nano 12 (2018) 2539–2545.
[43] A. Ghosh, D. Paria, H.J. Singh, et al., Dynamical configurations and bistability of helical nanostructures under external torque, Phys. Rev. E 86 (2012) 031401.
[44] T. Petit, L. Zhang, K.E. Peyer, et al., Selective trapping and manipulation of microscale objects using mobile microvortices, Nano Lett. 12 (2012) 156–160.
[45] S. Klumpp, C.T. Lefèvre, M. Bennet, et al., Swimming with magnets: From biological organisms to synthetic devices, Phys. Rep. 789 (2019) 1–54.
[46] E.M. Purcell, Life at low Reynolds number, Am. J. Phys. 45 (1977) 3–11.
[47] P. Dhar, C.D. Swayne, T.M. Fischer, et al., Orientations of Overdamped Magnetic Nanorod-Gyroscopes, Nano Lett. 7 (2007) 1010–1012.
[48] S. Broersma, Viscous force and torque constants for a cylinder, J. Chem. Phys. 74 (1981) 6989–6990.
[49] S. Broersma, Viscous Force Constant for a Closed Cylinder, J. Chem. Phys. 32 (1960) 1632–1635.
[50] S. Broersma, Rotational Diffusion Constant of a Cylindrical Particle, J. Chem. Phys. 32 (1960) 1626–1631.
[51] T. Li, A. Zhang, G. Shao, et al., Janus Microdimer Surface Walkers Propelled by Oscillating Magnetic Fields, Adv. Funct. Mater. 28 (2018) 1706066.
[52] T.Y. Chiang, D. Velegol, Localized electroosmosis (LEO) induced by spherical colloidal motors, Langmuir 30 (2014) 2600–2607.